

# Wide Bandwidth Time-Domain Electromagnetic Sensor for Metal Target Classification

Carl V. Nelson, *Member, IEEE*, Charles B. Cooperman, Wolfer Schneider, Douglas S. Wenstrand, and Dexter G. Smith, *Senior Member, IEEE*

**Abstract**—A portable, wide bandwidth, time-domain electromagnetic sensor system has been developed and used extensively to measure the eddy current time-decay response of a wide variety of metal targets. The sensor has demonstrated the ability to measure metal target decay times starting approximately 3 to 5  $\mu$ s after the transmitter current is turned off and target decay time constants as short as 1.4  $\mu$ s. The sensor has demonstrated the potential for detecting very low-metal content mines due to the void they create in some types of electrically lossy soils. The development of the sensor is described in detail, and time-decay data are shown for a variety of metal targets, including low metal antitank and antipersonnel mines.

**Index Terms**—Clutter reduction, electromagnetic induction, identification, landmine, magnetic transducers, metal detection, object detection, time-domain measurements.

## I. INTRODUCTION

**W**ITH an estimated 100 million mines worldwide [1], there is a need for sensor systems that can detect and identify large and small metal objects buried in soil. A commonly used sensor for mine detection is the electromagnetic induction (EMI) metal detector. Current state-of-the-art EMI metal detectors can detect small metal objects at shallow depths and large metal objects at deep depths under a wide range of environmental and soil conditions. However, metal nonmine (clutter) objects commonly found in the environment are a major issue for mine remediation [2], [3]. Because these clutter objects represent false targets, they create a false alarm (potential mine) when detected by a metal detector. For time-efficient and cost-effective land clearing, the detected metal targets must be classified as to their threat potential: mine or clutter. This article describes an electromagnetic target discriminator (ETD) sensor that shows potential for discriminating metal mines from clutter.

The ETD sensor is a wideband, time-domain sensor system with an impulse-function system response. Developed as a research tool to better understand the physics of EMI metal classification, it provided a proof-of-concept for mine discrimination in different soil types. Test targets investigated in this research range from large metal antitank (AT) mines and common anthropic metallic clutter to low metal plastic AT and antiper-

sonnel (AP) mines. In addition, the ETD sensor has shown potential for detecting very low-metal content mines due to the void they create in some types of electrically lossy soils [4].

Fig. 1 shows a simplified diagram of the basic pulsed-EMI technique. A current loop transmitter is placed in the vicinity of the buried metal target, and a steady current flows in the transmitter for a sufficiently long time to allow turn-on transients in the soil (soil eddy currents) to dissipate. The transmitter loop current is then turned off. According to Faraday's Law, the collapsing magnetic field induces an electromotive force (emf) in nearby conductors. This emf causes eddy currents to flow in the conductor. Because there is no energy to sustain the eddy currents, they begin to decrease with a characteristic decay time that depends on the size, shape, and electrical and magnetic properties of the conductor [5], [6]. The decay currents generate a secondary magnetic field, the time rate-of-change of which is detected by a receiver coil located above the ground.

Extensive theoretical and experimental research supports the concept of metal object classification using EMI techniques. Both frequency-domain and time-domain sensors have been proposed, studied, analyzed, and tested [5]–[15]. The ETD sensor builds on this previous research in an attempt to extend the range of metal content and depth capability of an EMI metal target classification sensor.

In the time-domain, the eddy current time-decay response from a metal target can be expressed as

$$V(t) = \delta(t) - \sum_i [A_i \exp\{t/\tau_i\}] \quad (1)$$

where

- $t$  time;
- $V(t)$  induced voltage in the receiver coil;
- $\delta(t)$  delta function;
- $A_i$  target amplitude response coefficients;
- $\tau_i$  target's time constants.

Thus, the sensor response to a metal target is a sum of exponentials with a series of characteristic amplitudes,  $A_i$ , and time constants,  $\tau_i$ . Equation (1) forms the theoretical basis of an EMI sensor's classification technique.

As earlier work has suggested, if a target is shown to have a unique time-decay response, a library of potential threat targets can be developed. When a metal target is encountered in the field, its time-decay response can be compared to those in the library and, if a match is found, the target can be classified. The best method of using the time-decay response in an automatic target recognition algorithm to classify targets is an area of active research [12], [16] and will not be addressed in this report.

Manuscript received July 1, 2000; revised October 1, 2000. This work was supported by the U.S. Army CECOM, NVSED, under Contract DAAB07-97-C-6041.

The authors are with the Applied Physics Laboratory, The Johns Hopkins University, Laurel, MD 20723-6099 USA (e-mail: carl.nelson@jhuapl.edu; chuck.cooperman@jhuapl.edu; dexter.smith@jhuapl.edu).

Publisher Item Identifier S 0196-2892(01)05111-7.

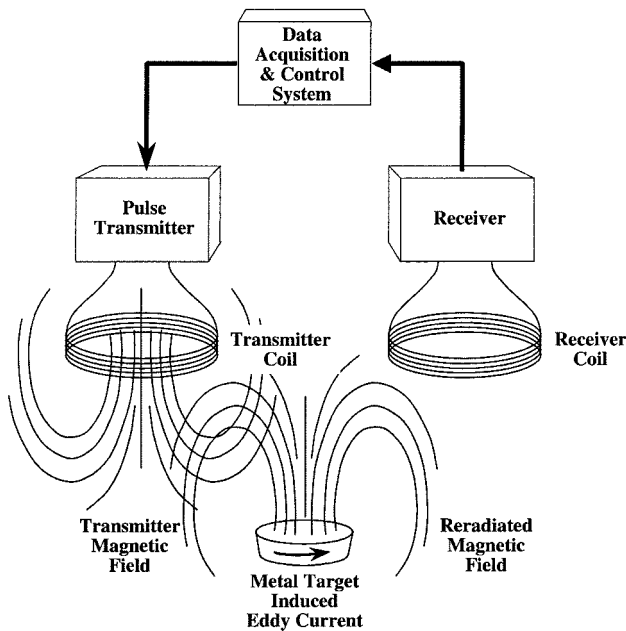


Fig. 1. Simplified diagram of the basic pulsed-EMI metal detection technique.

This report will focus on the sensor (Section II) and results from recent laboratory and field measurements (Section III).

## II. SENSOR DESCRIPTION

### A. Sensor Electronic Design

The objective of developing the ETD sensor was not to develop an optimized, metal target-searching, commercial stand-alone product, but to develop a research tool for investigating time-decay response characteristics of a variety of metal targets. To this end, the sensor was designed to be modular in nature: the sensor electronics are general purpose and can be used with a variety of transmitter and receiver coil configurations. Fig. 2 shows a simplified block diagram of the ETD sensor. The sensor is composed of a computer-controlled current source feeding a transmitter switch, a current sense amplifier for setting the transmitter coil current, a transmitter coil, two receiver coils, multistage, high-bandwidth receiver coil amplifiers, and a high-speed portable data acquisition system (DAS) controlled by a single-board computer.

Selected features of the sensor electronic systems are summarized as follows.

- The transmitter is similar to an H-bridge drive used in single polarity, bipolar motor controls. The main drive circuit component is an insulated gate, bipolar transistor (IGBT). The IGBT has a 600 V breakdown voltage that makes it ideal for switching highly inductive loads characteristic of multiturn pulse-EMI transmitter coils.
- The receiver coil preamplifier is a low-noise, wide-band differential transconductance amplifier (Maxim MAX-4146).
- A computer data acquisition system based on the PC/104 standard (IEEE-P996 Standard) performs data acquisition, control, data storage, and display functions. The computer

controls the analog-to-digital converter (ADC) board operation, pulse repetition rate of the transmitter, transmitter current, data averaging, and data display.

- Receiver coil data were digitized by a 12-bit, 10-Msample/s ADC.
- A head-mounted video display allows the operator to view each data collection graphically. This allows the operator to verify data quality and ensure that all sensor parameters were set correctly.
- A rechargeable lithium-ion battery powers the sensor for about 6 h.
- Excluding the transmitter and receiver coils, the total weight of the sensor with batteries is about 4 kg.

One data scan generates 8192 data values in the ADC board's memory buffer. At a sample rate of 10 Msamples/s, data are collected from 0.1  $\mu$ s to 819.2  $\mu$ s. If the number of scans is set to a number greater than one, the computer commands the ADC board to collect additional data until the preset number of scans is reached. For scans greater than one, the computer stacks the data in a one-dimensional (1-D) data array forming an ensemble average. After the preset number of scans is reached, the averaged data are plotted as voltage versus time for the operator to view. Data are saved to the computer's solid-state disk and can be transferred to a personnel computer for analysis and data archiving.

A typical data collection operation involves five basic steps: setting sensor data collection parameters, placing the sensor over a target of interest, performing data acquisition, saving data to disk, and repeating the whole procedure and collecting a background reading. Background data are collected over an area that is nearby but is known to not have a metal target. During data analysis, the background is subtracted from the target data. This procedure accomplishes two things: it removes any amplifier offset voltage drift and any residue decay currents from the transmitter coil that are coupled into the receiver coil. For medium and large targets, the background subtraction procedure produced minimal differences in the time-decay response curves because the sensor's drift and the residue currents in the transmitter coil are orders of magnitude below the target's time-decay response voltage. However, for small targets, at decay times close to the transmitter shut off time, the background subtraction procedure does improve the quality of the data. The level of improvement is difficult to quantify because it is dependent on target size, metal content, metal type, target-to-sensor distance, and soil type. The goal of future sensor designs is to improve the amplifier offset stability and reduce the effect of residue transmitter current in the receiver coil.

### B. Transmitter and Receiver Coil Design

As with frequency-domain EMI sensors [11], the development of an antenna (transmitter and receiver coil combination) for a time-domain sensor is somewhat of an art form. Performance tradeoffs and compromises are made between antenna size, target depth, mechanical and electrical complexity, bandwidth, sensitivity, and mechanical ruggedness. The ETD antennas described in this paper have by no means been completely optimized for all of these characteristics. However, two

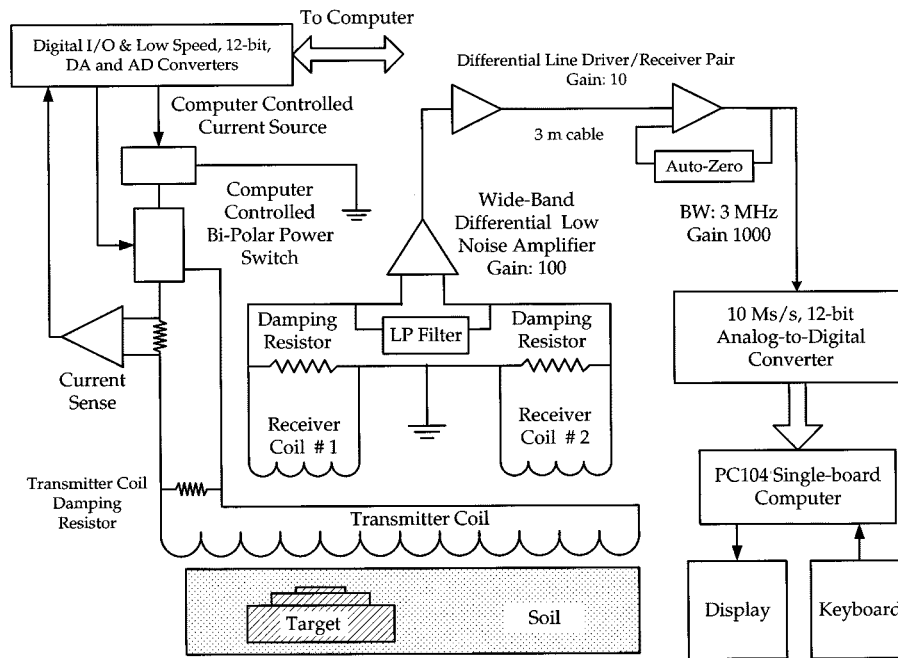


Fig. 2. Simplified block diagram of ETD sensor.

baseline antennas were developed that satisfied the primary goal of measuring the time-decay response of a wide range of metal targets at typical mine depths (surface to about 15 cm). During this research effort, a small antenna was constructed for small metal targets and a larger antenna was constructed for large metal targets.

The initial laboratory target testing established that a multi-turn antenna was needed for adequate time-decay measurement sensitivity. Also, it was experimentally determined through examination of time-decay data from many medium and large metal targets that data collection should start at least 10 to 20  $\mu$ s after transmitter shutoff.

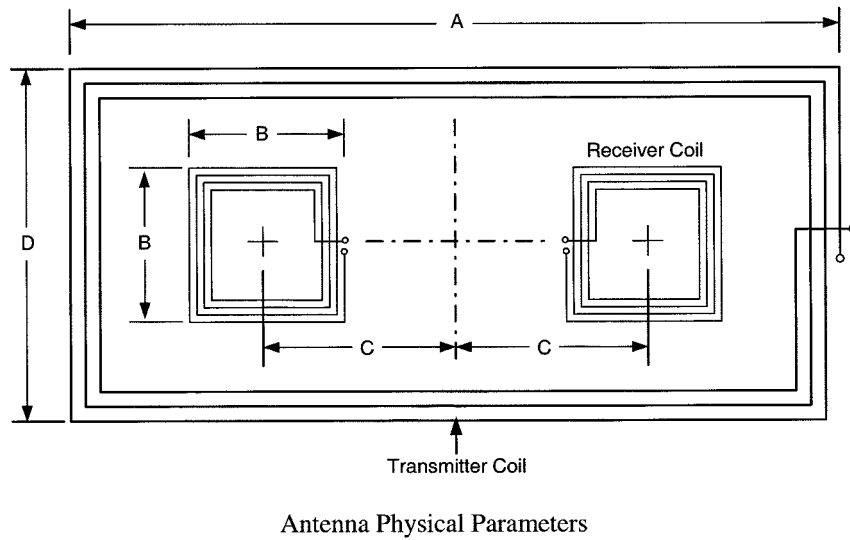
When current is switched off in an inductor it takes a finite amount of time for the currents to decay to zero. Large multi-turn transmitter coils tend to have high inductance and when the current is switched off, their long decay time currents tend to mask induced target decay currents. The technique used to minimize the effects of slowly decaying currents in the transmitter coil borrows ideas from the well-established technique of the balanced bridge. Conceptually, the technique (refer to Fig. 2) involves placing the target coil (coil 1) over the unknown metal object. The second coil (coil 2) sits over soil that does not contain metal. Coil 1 measures the time decay of the metal target, time decay of the soil, and transmitter coil decay currents. Coil 2 measures the time decay of the soil and transmitter coil decay currents. The differential amplifier subtracts the two coil signals, and the result is an output of just the metal target decay signal.

The separation distance between the two receiver coils is an important design parameter. Ideally, the magnetic flux from the target should link only with the receiver coil directly above it. Flux linkage with the second receiver coil should be minimized. For extended source targets (those represented by large metal mines), the separation of the two receiver coils is important. If

the two receiver coils and the large target are viewed as forming a loosely coupled transformer, it is easily seen that the mutual inductance of target and the second balance receiver coil should be minimized. The easiest method to achieve this result is to physically separate the two receiver coils. Experiments showed that if the receiver coil was made approximately the size of the largest target of interest, the two receiver coils should be separated at least one receiver coil diameter apart. This rule-of-thumb was developed in the early phase of ETD antenna development and appeared to work for extended targets to depths of about 20 cm. To reduce the coupling effect further, subsequent antenna designs had smaller diameter receiver coils and separation distances at least two or more receiver coil diameters apart.

As with many magnetic field sensor designs based on induction coils, the differential receiver coil design is a compromise over a perfect point magnetic field sensor. As a target-to-sensor distance  $R$  increases relative to the differential receiver coil separation distance  $D$ , the differential receiver coil arrangement loses its effectiveness. To understand this effect, consider a simple target modeled as a point source dipole directly under receiver coil 1 at distance  $R_1$ . The signal seen by receiver coil 1 is approximately proportional to  $R_1^{-3}$ , and the signal seen by receiver coil 2 is approximately proportional to  $R_2^{-3} = (D^2 + R_1^2)^{-3/2}$ . As the distance from the target to the plane of the receiver coils increases,  $R_1$  becomes large relative to  $D$ , and  $R_2$  approaches  $R_1$ . The field strength seen by both receivers becomes nearly equal. The differential arrangement of the two coils then tends to cancel the signal.

The balanced two-receiver coil technique worked well for minimizing the transmitter decay current and offered two additional benefits: transmitter-induced ground eddy current signal cancellation and far-field noise cancellation. For the large metal target work done during the initial phase of the research, the ground eddy current signal was not a source of significant inter-



Antenna	A cm	B cm	C cm	D cm	Transmitter loop turns	Receiver loop turns
Small	60	10	20	21	8	16
Large	100	15	27	58	6	16

Fig. 3. ETD antenna physical parameters.

ference. However, as the target size became smaller, the ground eddy current signal became more important. The balanced receiver coil configuration tends to minimize the effect of the ground, and allows the sensor to operate close to highly conductive and magnetic soils. Additionally, the balanced receiver coil arrangement tends to cancel the electrical noise generated from nearby electrical equipment. The receiver coil still picks up electrical noise sources, but the electrical noise does not saturate the sensor's amplifier. With ensemble averaging, the sensor can function in a conventional laboratory environment in the presence of power line and equipment noise.

Fig. 3 summarizes the design and physical dimensions of two antennas developed for the ETD sensor. The measured antenna electrical parameters are the following.

- Small transmitter coil:

$$R = 1.8 \, \Omega, \quad L = 69 \, \mu\text{H}, \quad C = 240 \, \text{pF}, \quad F_r = 1.1 \, \text{MHz}.$$

- Small receiver coil:

$$R = 4.5 \, \Omega, \quad L = 50 \, \mu\text{H}, \quad C = 197 \, \text{pF}, \quad F_r = 1.6 \, \text{MHz}.$$

- Large transmitter coil:

$$R = 2.2 \, \Omega, \quad L = 60 \, \mu\text{H}, \quad C = 382 \, \text{pF}, \quad F_r = 1.1 \, \text{MHz}.$$

- Large receiver coil:

$$R = 2.1 \, \Omega, \quad L = 27 \, \mu\text{H}, \quad C = 555 \, \text{pF}, \quad F_r = 1.3 \, \text{MHz}.$$

where  $F_r$  is the resonance frequency.

To document the performance of these antennas, several calibration targets were constructed from a single turn of thin copper wire [17]. These calibration targets have a time-decay response that can be calculated analytically from theory. The calibration target's time-decay response was then measured with the two antennas and compared to the theoretical response.

Fig. 4 shows a sample time-decay response from the different calibration loops for the small ETD antenna. The diameter of the calibration loops were made large (about 8.5 cm) so that the effective dipole moments of the loops gave a high SNR at the receiver. A nonlinear least-squares method [18] was used to fit the time-decay response data to a single exponential-term equation. The figure shows that the curve-fitted data (time-decay parameter) and calculated decay times are exact for the small antenna up to  $1.4 \, \mu\text{s}$ . Similar results were obtained for the large antenna but with a reduced time response of about  $2 \, \mu\text{s}$ . The results of the time constant calibration gives confidence that the sensors are measuring accurate target time-decay responses.

### III. TIME DECAY RESPONSE MEASUREMENTS

#### A. Data Presentation

If a target's time-decay response can be shown to be unique, target classification is one step closer to reality. One data presentation method to show a target's uniqueness is to plot the data graphically as a function of time. The primary objective of presenting data in this manner is to show the distinct nature of a target's response compared to other targets. The time-decay response is an inherent property of the target. Once excited by the sensor's transmitter coil, the target's magnetic field decays uniformly in space. The absolute amplitude of the time-decay response does not govern the target characterization process. In some cases, in order to show more clearly the differences in the relative time-decay rates of targets with large differences in absolute amplitude responses, the time-decay data amplitudes have been normalized to 1 at some convenient time. For the cases of small metal targets, the amplitude information is important to show relative signal strength, and for those cases the data are not normalized.

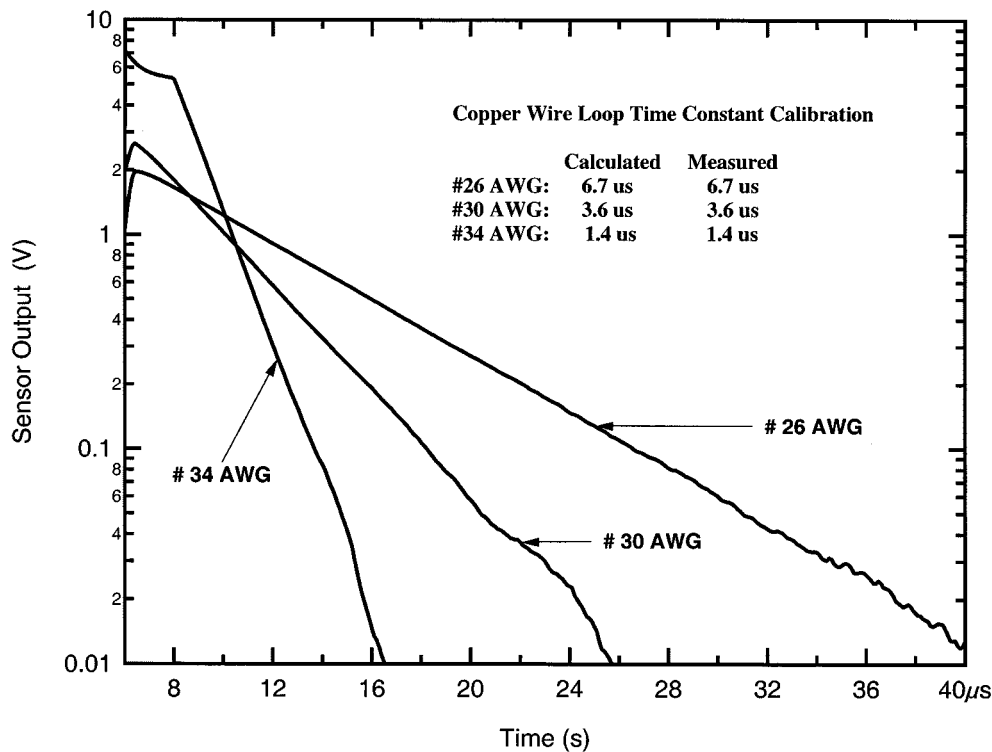


Fig. 4. Calibration time-decay data for small ETD antenna.

### B. Large Metal Target Data

Target tests were conducted at our laboratory and at government test sites. Data were collected from a wide variety of metal test targets. The tests were conducted in air using steel and non-ferrous plates and rings from 10 to 30 cm in diameter, common clutter targets such as soda and paint cans, hand tools, typical battlefield clutter, and large metal mines. For the over 100 targets studied, the time-decay response data showed that different metal targets had unique time-decay response signatures.

Fig. 5 shows sample time-decay response data (normalized at 15  $\mu$ s) from various medium and large metal targets measured by the large ETD antenna. The figure shows data from targets common in a battlefield environment: a cartridge clip from an M16 rifle, various mortar and gun shell casings, a large undefined ferrous clutter object, a VS50 AP mine, and an air-deployed U.S. Army Gator AT mine without its MS plates. The targets were measured in air at various distances from and at various orientations (vertical and horizontal) to the sensor antenna. In all cases, signal processing of the data was not needed to differentiate the different targets. A visual examination of the time-decay plots was sufficient for discrimination.

Tests were also conducted to investigate the effects of different soil types on large metal target time-decay responses. When compared to measurements made in air, no significant differences were found in the time-decay responses for large metal targets buried in dry gravel, sand, or clay soils. However, small time-decay response differences were found in the highly magnetic soil used in one of the indoor mine lanes [19]. In order to estimate the magnetic soil effect, time-decay response data from two different metal AT mines (TM46 and FFV028) were compared to data taken in dry clay and magnetic sand. The compar-

ison was made by parameterizing the time-decay curves using a single exponential curve fit [18] over a time window from 300  $\mu$ s to 800  $\mu$ s. Over this time window, the goodness of fit parameter  $\chi^2$  was approximately  $10^{-3}$ . The time-decay fit parameter for the two different soil types and two different mines differed by approximately 2 to 5%.

One interesting result of these metal mine tests was that mines with very similar construction (material, size, and shape) showed measurable differences in their time-decay responses. Although these differences can be seen in a plot of time-decay data, the subtle time-decay features can more clearly be seen if the general time-decay trend is removed from the data. The TM46 AT mine was selected as a reference time-decay signal. After normalizing all target responses at 50  $\mu$ s, the time-decay response of the TM46 AT mine was subtracted from the other large metal targets. The time-decay differences are shown in Fig. 6. The plot clearly shows subtle but measurable differences between large metal AT mines. The figure also shows a sensor glitch at about 1 ms caused by the transmitter timer signal coupling into the receiver circuit. The problem was traced to a broken ground wire in the transmitter cable shield.

### C. Metal and Void Data

Fig. 7 shows results from one of the more interesting test targets. These data were taken in magnetic sand. The figure shows time-decay responses from four different test configurations: a decommissioned nonmetallic-cased Russian PMN AP mine (11-cm diameter, 5.6-cm height; with about 40 g of interior ferrous and nonferrous metal components) in air, a hole in the sand, a simulated plastic mine with no metal parts buried in the sand, and the PMN AP mine buried in the sand. The following mea-

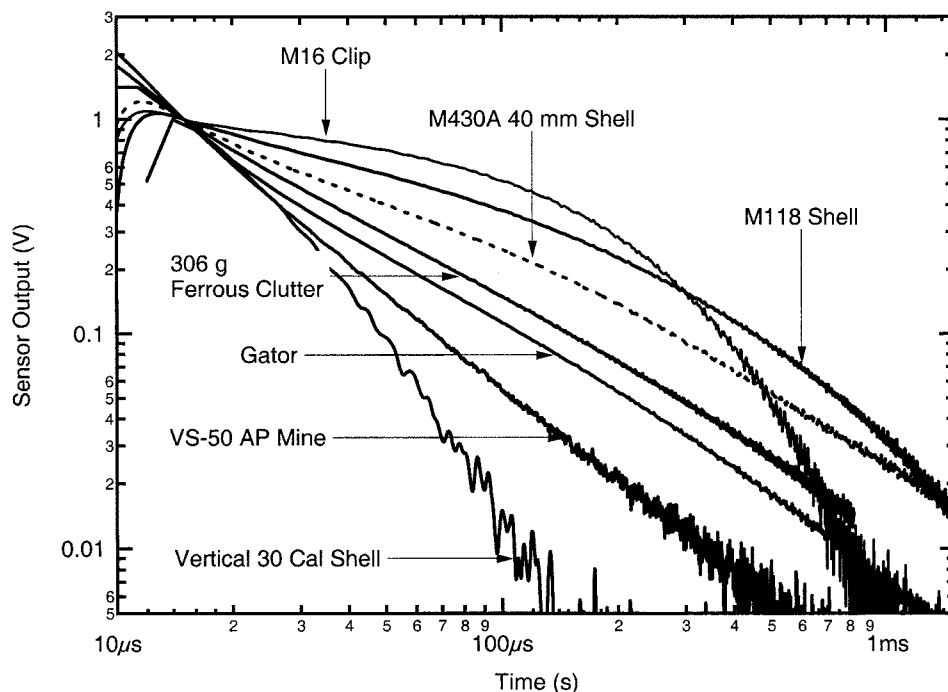


Fig. 5. Time-decay response from M16 clip, VS50 AP mine, M430A 40 mm shell casing (vertical orientation), M118 shell casing (vertical orientation), 306-g ferrous clutter, Gator air-deployed mine without MS plates, and 30-cal shell casing (vertical orientation). Target measurements made in air with large ETD antenna. Data is normalized at  $15 \mu\text{s}$ .

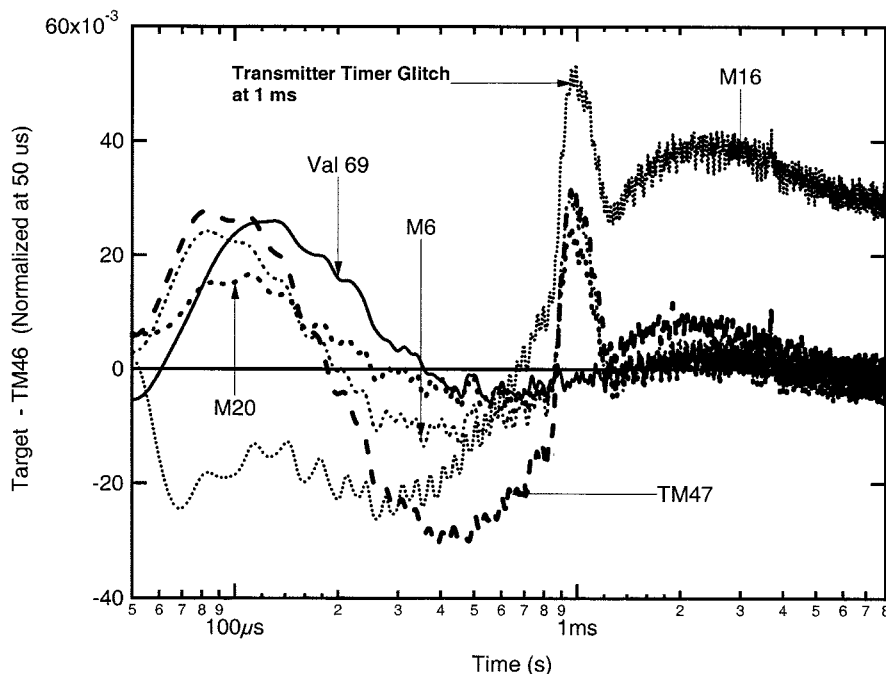


Fig. 6. Time-decay response of various AT metal mines relative to a TM46 AT metal mine. Data normalized at  $50 \mu\text{s}$ .

measurements were taken with the sensor centered over the test area approximately 5 cm above the sand surface.

- 1) The time-decay response of the PMN mine sitting on the surface of the magnetic sand (in air). The time-decay signal starts out positive and decays to zero. The differential receiver coil arrangement cancels the sand's time-decay response. This shows the sensors ability to operate in soil conditions with high magnetic/conductive properties.

- 2) A hole approximately 12 cm deep and 12 cm in diameter was dug in the magnetic sand. The time-decay response of the hole was measured. Because of the differential geometry of the ETD antenna, the hole or void creates an amplitude response opposite that of the metal (in this case negative). Note the time scale of this response: the sand's time-decay response occurs primarily in the less than  $10\text{-}\mu\text{s}$  region. Also, the amplitude response of the hole is fairly large (approximately 1.3-V maximum am-

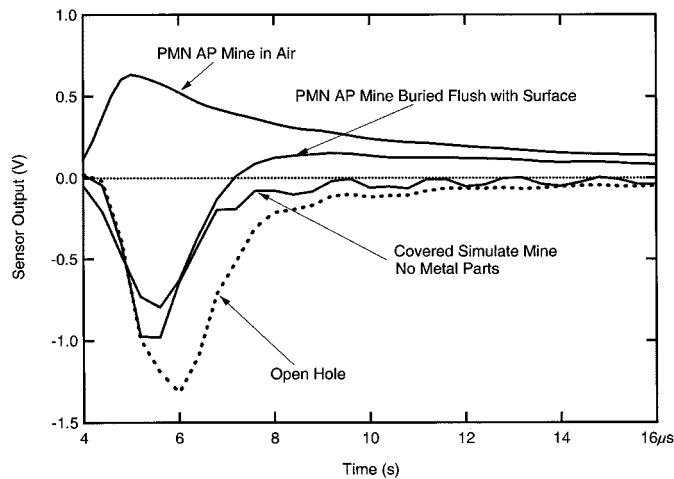


Fig. 7. Time-decay response of various targets buried in a magnetic soil showing the void effect: open hole, covered simulated mine, buried PMN AP mine, and a PMN AP mine setting on the surface.

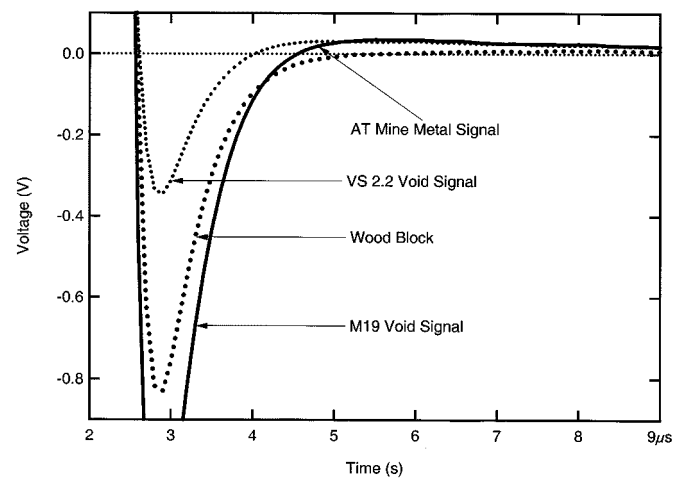


Fig. 8. Time-decay response from a block of wood, and two LMC AT mines: M19 and VS 2.2. Data measured with small ETD antenna.

plitude) and goes from negative to zero amplitude. The large voltage signal from the sensor was repeatable and indicates that the negative response was not a sensor or background subtraction artifact.

- 3) Next, a simulated plastic mine (approximate size of the PMN mine) was placed in the hole and covered with about 1 cm of magnetic sand. Its time-decay response was measured and showed a small reduction in amplitude compared to the hole by itself. The simulated mine's response also varies from negative amplitude to zero.
- 4) Finally, the PMN mine was buried in the magnetic sand, with the top of the mine approximately 1 cm below the surface. Its time-decay response can be divided into two regions. In the time region just after transmitter turn-off, where the hole time-decay response dominates, the sensor measures the hole or void created by the relatively large volume of displaced magnetic sand. The second time region (after about 8  $\mu$ s) is dominated by the time-decay response from the mine's metal parts.

Additional laboratory tests with simulated mines in wet and dry topsoil showed results that were similar to those shown in Fig. 7 but with greatly reduced signal amplitude: a void signal with a coincident metal signature.

#### D. Low-Metal Target Data

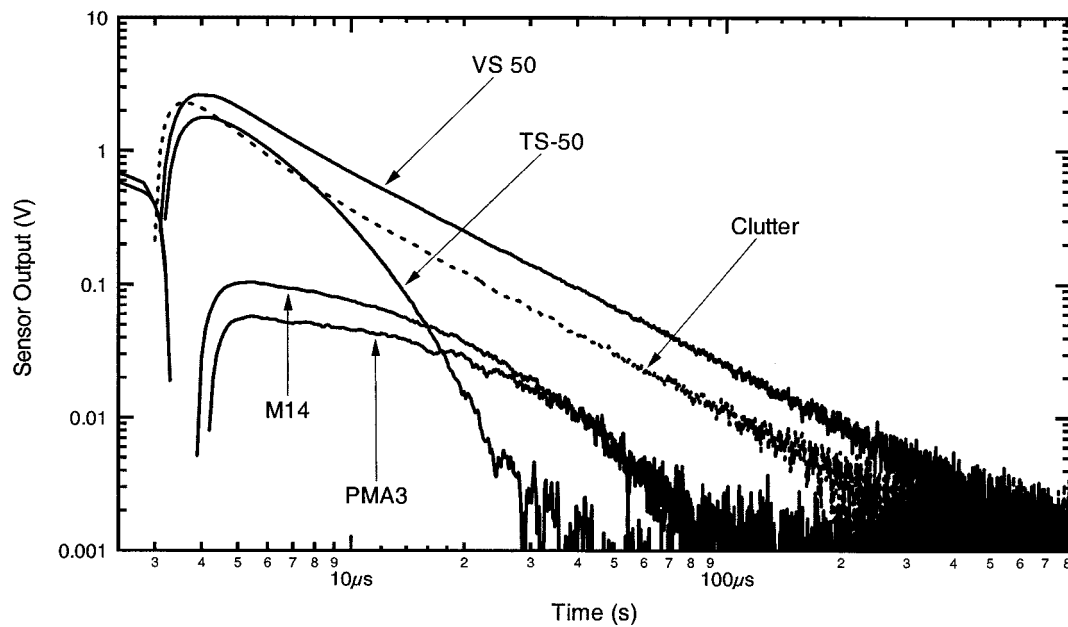
A test with buried low metal content (LMC) AP and AT mines under field conditions was conducted in October 1999. The two primary objectives of this test were 1) to ascertain whether the laboratory void results with simulated LMC mines could be confirmed under field conditions with real LMC mines and 2) to collect and compare data from clutter and LMC AP and AT mines.

The coincident void/metal results discussed in Section III-C were confirmed during this test. As an example, Fig. 8 shows a plot of the time-decay response from a block of wood and two LMC AT mines (M19 and VS 2.2). The targets were buried in the same soil type (sandy loam) and data were collected with the small EDT antenna centered about 4 cm above the ground. The figure lists the target parameters and burial depths. A void

signal is clearly evident in the plot from each target. However, a small but discernible metal signal is present from the M19 and VS 2.2 AT mines due to their metal components. The void response of the wood target decays to zero and never indicates a metal signature (positive voltage). These results appear to confirm the earlier test results with the PMN mine in the magnetic sand and show that under certain soil conditions and with some mine types, a nonmetallic-cased mine with metal content potentially may be identified by its void and coincident metal signature.

Fig. 9 shows a log-log plot of time-decay data for four AP mines and a ferrous clutter target measured by the small ETD antenna centered 4 cm above the ground. The figure lists the target parameters, burial depths, and estimates of time decays using a single exponential fit to the data over the time window 7 to 50  $\mu$ s. The plots show that the M14, and PMA3 AP mines have different time-decay response curves. Note also that the M14 and PMA3 appear to have a small void effect component in the time period between 3 and 4  $\mu$ s where the response curves dip toward negative response. The VS50 AP mine is easily detected via its 18-g steel blast-effect disk. The steel disk is used to enhance its lethality at the expense of detectability. The VS50 (time-decay estimate: 6.5  $\mu$ s) and the 16-g ferrous clutter (time-decay estimate: 5.8  $\mu$ s) present very similar time-decay responses, making discrimination on this parameter alone difficult. The TS50 AP mine has a relatively large amplitude response but decays very rapidly (time-decay estimate: 3.2  $\mu$ s). Because of the fast decay time, this mine is very difficult to detect with a conventional EMI metal detector [20].

Fig. 10 explores the time-decay response of the M14 AP mine in more detail. The figure compares the time-decay response of an M14 in air and buried in soil with the response of two small steel metal clutter targets. The data were measured by the small ETD antenna centered 4 cm above the ground. The most obvious feature to note is the dissimilar time-decay responses of the in air and buried M14 mines during the early part of the time decay. The in-air and buried time decays appear to merge in the late time region (after about 20  $\mu$ s). It is theorized that the differences in the early time response are due to the void



Target	Size: mm Diameter x Height	Metal Weight/Type g	Burial Depth cm	Time Constant 1* μs
VS-50	90 x 45	18 : ferrous	5	6.5
Clutter	unknown	16 : ferrous	3	5.8
TS-50	90 x 45	4.4 : non-ferrous	surface	3.2
M14	56 x 40	0.6 : non-ferrous	0.6	13
PMA3	111 x 40	0.35 : non-ferrous	surface	19

\* Data fitted to a single exponential over time window: 7 to 50 μs

Fig. 9. Time-decay response from buried M14, PMA3, VS50, and TS50 AP mines, and 16-g ferrous clutter target. Data measured with small ETD antenna.

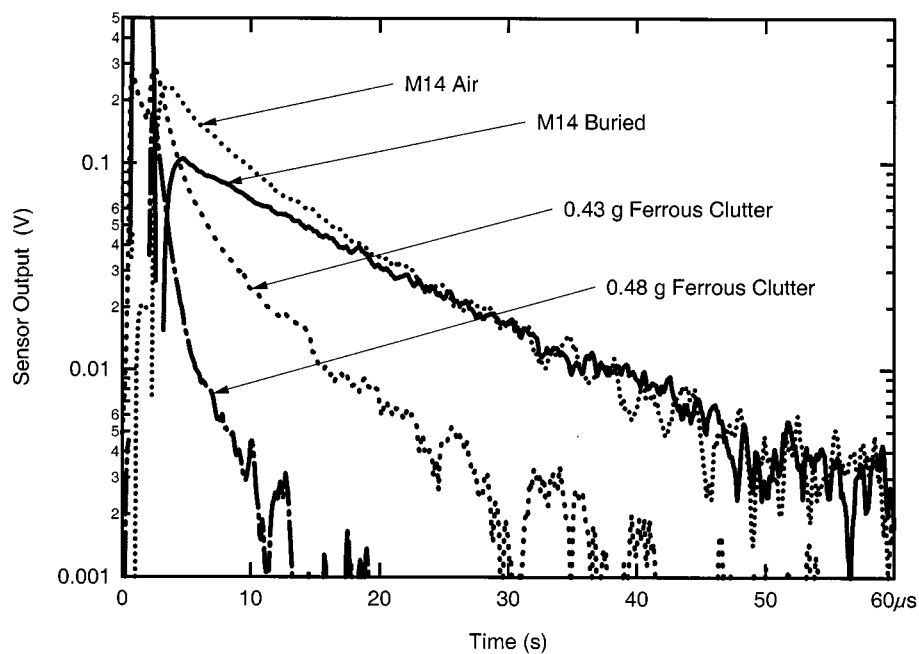


Fig. 10. Time-decay responses of an M14 in-air and buried in soil plus the responses of two small steel metal clutter targets. Data measured with small ETD antenna.

effect created by the M14 in the soil. In the late time region, the response of the ground has decayed to a small value and has minimal effect on the remaining portion of the M14's time decay.

Fig. 10 also compares the M14 to two small ferrous metal clutter objects with metal weights similar to the M14's metal content. The clutter objects are bare metal parts of different shape found during the test range preparation and replaced in



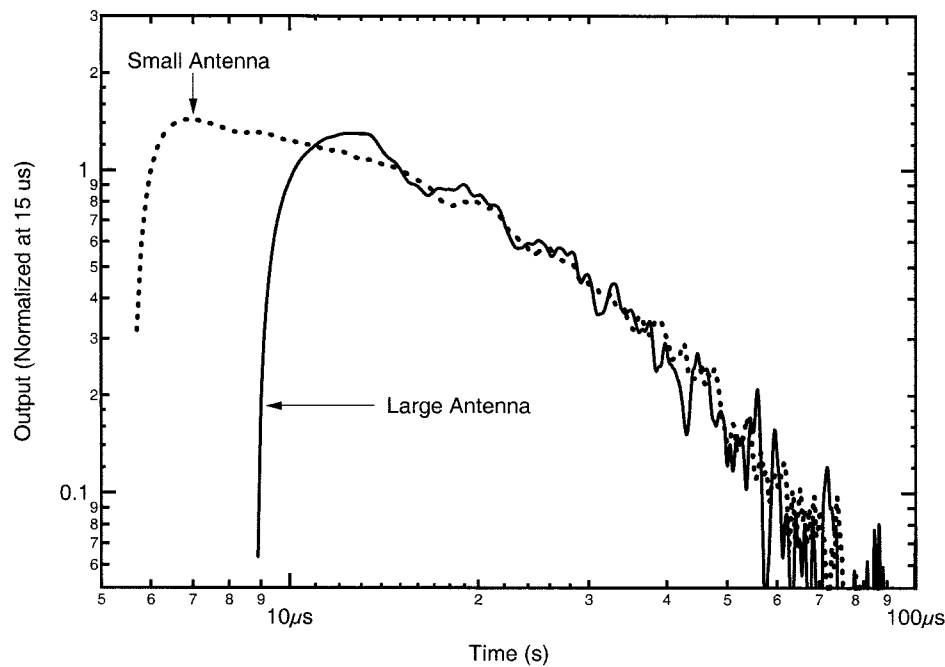


Fig. 11. Comparison of time-decay response from a buried PMA3 AP mine measured by the large and small ETD antennas.

the ground at a known depth. The first item to note in the figure is that the ferrous clutter objects have very different time-decay responses compared to the M14 mine. This would be expected since the M14, like most LMC mines, uses small amounts of both ferrous (e.g., firing pin) and nonferrous (e.g., firing pin support cup) metal components. Also note that even though the two ferrous clutter targets have approximately the same metal weight, they have different time-decay responses. A third item to note is the metal clutter appears to have no void response compared to the buried M14 AP mine (i.e., a dip in the response voltage around 3–4  $\mu$ s).

Fig. 11 compares the small and large ETD antennas over the same buried PMA3 AP mine. The data have been normalized at 15  $\mu$ s to show that the two antennas are measuring the same time-decay response in the time region beyond 15  $\mu$ s. However, the two antennas give different responses in the time region between approximately 5 and 10  $\mu$ s. The differences may be due to the way the two antennas respond to the void effect or an artifact of the slower frequency response of the larger antenna relative to the smaller antenna. One possible explanation may be due to the relative sizes of the two transmitter coils. We note that the large transmitter coil excites a much larger volume of soil compared to the small transmitter coil. The resulting eddy currents from the soil cause a larger imbalance in the two receiver coils of the large antenna relative to the small antenna. The large antenna receiver coils may see the void more clearly possibly because of the increased volume of soil excited by the larger transmitter coil. This feature may hint to a method on designing a more complex antenna that senses both the void and metal signatures more effectively.

#### IV. CONCLUSION

We have shown that a time-domain sensor can be constructed with sufficient bandwidth and sensitivity to measure the time-

decay response of large metal objects and LMC AP and AT landmines buried at typical burial depths. Time-decay responses from targets with metal content from more than 3000 g to less than 1 g were demonstrated. The sensor has demonstrated the ability to measure metal target decay times starting approximately 3 to 5  $\mu$ s after the transmitter current is turned-off and target decay time constants as short as 1.4  $\mu$ s.

We have also presented results from laboratory and field tests which indicate that medium and large metal content mines have unique time-decay response characteristics that will allow them to be discriminated from a wide variety of typical metal clutter in a variety of soil types. As Fig. 6 indicates, large metal targets have many complex structural features that manifest themselves in different time-decay characteristics. At least for nonmagnetic soils, the soil decay response appears to have little influence on an EMI sensor. For medium and large metal targets, highly magnetic soils appear to have minimal impact on the target's decay response (less than 5%).

An issue that is still an open question is whether one can discriminate LMC mines from LMC clutter by comparing their time-decay responses. Although this research demonstrates the potential to discriminate between LMC ferrous clutter and nonferrous LMC mine metal components, more data need to be gathered. One of the issues highlighted in Figs. 7 and 10 is the fact that the time-decay response of a mine is modified by the soil response. The measured response is a superposition of the target's metal component response and the response of the soil. The small and large antenna comparison in Fig. 11 shows that this superposition of responses is dependent on the sensor's antenna configuration. In addition, because in most cases the soil effects are not known in advance, the time-decay character of an LMC mine may be masked by the unknown soil response. The soil's effect on an LMC mine's decay response will make it difficult to develop a robust, universal library of target signatures.

However, we have shown that the ETD sensor has the potential ability to measure both the metal and the void signature of the LMC mines in some soil types. The existence of a coincident void and metal signal may hold promise of a robust LMC mine classification/discrimination scheme. Exploiting this potential capability is the subject of current research at our laboratory.

## REFERENCES

- [1] "Report to the Secretary of Defense on the status of Department of Defense's implementation of the United States policy on anti-personnel landmines," Office of the Under Secretary of Defense for Policy, Washington, DC, May 1997.
- [2] J. Goutsias, "Toward a unifying optimal approach to mine detection problems," *Proc. SPIE*, vol. 2765, 1996.
- [3] E. Gelenbe and T. Kocak, "Area-based results for mine detection," *IEEE Trans. Geosci. Remote Sensing*, vol. 38, pp. 12–24, Jan. 2000.
- [4] T. Yu and L. Carin, "Analysis of the electromagnetic-inductive response of a void in a conducting-soil background," *IEEE Trans. Geosci. Remote Sensing*, vol. 38, pp. 1320–1327, May 2000.
- [5] A. A. Kaufman, "Frequency and transient responses of electromagnetic fields created by current in confined conductors," *Geophysics*, vol. 43, pp. 1002–1010, 1978.
- [6] C. E. Baum, "Low-frequency near-field magnetic scattering from highly, but not perfectly, conducting bodies," Phillips Labs. Interaction Note 499, Nov. 1993.
- [7] Y. Das, J. E. McFee, and D. R. H. Cherry, "Time-domain response of a sphere in the field of a coil: Theory and experiment," *IEEE Trans. Geosci. Remote Sensing*, vol. GE-22, pp. 360–367, July 1984.
- [8] Y. Das and J. E. McFee, "A simple analysis of the electromagnetic response of buried conducting objects," *IEEE Trans. Geosci. Remote Sensing*, vol. 29, pp. 342–344, Mar. 1991.
- [9] G. D. Sower and S. P. Cave, "Detection and identification of mines from natural magnetic and electromagnetic resonances," *Proc. SPIE*, vol. 2496, 1995.
- [10] J. D. McNeill and M. Bosnar, "Application of time domain electromagnetic techniques to UXO detection," in *Proc. UXO Forum 1996*, 1996, pp. 34–42.
- [11] I. J. Won, D. A. Keiswetter, and D. R. Hanson, "GEM-3: Monostatic broadband electromagnetic induction sensor," *J. Environ. Eng. Geophys.*, vol. 2, pp. 53–64, March 1997.
- [12] D. D. Snyder, S. MacInnes, S. Urquhart, and K. L. Zonge, "Possibility for UXO classification using characteristic modes of the broad-band electromagnetic induction response," in *Proc. New Technology Applications Conf. Science and Technology of Unexploded Ordnance Removal and Site Remediation*, Maui, HI, November 8–11, 1999.
- [13] P. Kaczowski and D. Gill, "Pulsed electromagnetic induction as a UXO detection technology," in *Proc. UXO Forum 1996*, Williamsburg, VA, Mar. 26–28, 1996, pp. 43–52.
- [14] Y. Das, J. E. McFee, J. Toews, and G. C. Stuart, "Analysis of an electromagnetic induction detector for real-time location of buried objects," *IEEE Trans. Geosci. Remote Sensing*, vol. 28, pp. 278–288, 1990.
- [15] G. D. Sower, *Detection and Identification of Visually Obscured Targets*, C. E. Baum, Ed. London, U.K.: Taylor & Francis, 1999, pp. 243–282.
- [16] L. Collins, P. Gao, and L. Carin, "An improved Bayesian decision theoretic approach for land mine detection," *IEEE Trans. Geosci. Remote Sensing*, vol. 37, pp. 811–819, May 1999.
- [17] L. S. Riggs, L. T. Lowe, J. E. Mooney, T. Barnett, R. Ess, and F. Paca, "Simulants (decoys) for low-metallic content mines: Theory and experimental results," *Proc. SPIE*, vol. 3710, pp. 64–75, 1999.
- [18] D. W. Marquardt, "An algorithm for least-squares estimation of non-linear parameters," *J. Soc. Ind. Appl. Math.*, vol. 11, pp. 431–441, 1963.
- [19] L. S. Fontain, "Evaluation of the electromagnetic properties of soil materials," Final Tech. Rep. 0300.0127B, Southwest Res. Inst., Houston, TX, Dec. 5, 1984.
- [20] C. King, *Jane's Mines and Mine Clearance*. London, U.K.: Biddles, 1997.



**Carl V. Nelson** (M'01) received the B.A. degree in physics from California State University, Fullerton, in 1973, and the M.S. degree in engineering physics from the University of Virginia, Charlottesville, in 1975.

He is a Senior Staff Physicist with the Johns Hopkins University Applied Physics Laboratory (JHU/APL), Laurel, MD. He has 27 years of experience in sensor physics, oceanographic instrumentation and buoy systems, ocean optical modeling and instrumentation, electromagnetic modeling and instrumentation, signal processing and data analysis, and digital data acquisition systems. He holds several patents in instrumentation and sensor systems, and his current research interests are in mine and UXO detection, 3-D magnetic positioning sensors, and biomedical sensors.

Dr. Nelson is a member of Sigma Xi.



**Charles B. Cooperman** received the B.S. degree in 1982 in electrical engineering from The University of Maryland, College Park.

He is a member of the Senior Professional Staff, Johns Hopkins University Applied Physics Laboratory, Laurel, MD. His specialties include power systems, microcomputers, and analog and digital design. He is currently providing design support for a large oceanographic acoustic array system for the U.S. Navy.



**Wolfger Schneider** received the M.S. degree in electrical engineering from Drexel University, Philadelphia, PA, in 1966.

He is a member of the Principal Professional Staff, Johns Hopkins University Applied Physics Laboratory, Laurel, MD. For over 30 years, he has contributed to, conceived, and managed the design and construction of test equipment, data collection systems, and a variety of biomedical research systems. His specialties include analog and digital design as well as microcomputer and digital signal processing applications. He is the holder of four patents in the areas of data collection, digital control, and IR signaling as aids for the blind.



**Douglas S. Wenstrand** received the B.S. in electrical engineering from the University of Maryland, College Park, in 1994, and the M.S. in electrical engineering from The Johns Hopkins University, Baltimore, MD, in 1999.

As a Design Engineer for the JHU Applied Physics Laboratory, he has designed a wide variety of electronic systems for spacecraft, shipboard, biomedical, and military applications. His areas of interest include FPGA/ASIC design, embedded hardware and software design, C++ programming, and digital signal processing.



**Dexter G. Smith** (M'80–SM'90) received the B.S. and M.Eng. degrees in biomedical engineering in 1979 and 1980, respectively, and the M.Eng. and D.Eng. degrees in 1983 and 1984, respectively, in electrical engineering, all from Rensselaer Polytechnic Institute, Troy, NY.

He is a Member of the Principal Professional Staff, Johns Hopkins University Applied Physics Laboratory (JHU/APL), Laurel, MD. He has worked as a Clinical Engineer in a hospital setting and as a developer of consumer products utilizing active noise control, where he holds several patents. Since joining JHU/APL in 1995, he has been involved in signal processing and biomedical engineering. His current research interests include bioimpedance and acoustic signal processing. He also serves as the Vice Chair of the Part Time Electrical Engineering Master's Program at JHU.